Charge density wave and crystalline electric field effects in $TmNiC_2$

Marta Roman,[1,2,*] Maria Fritthum,[1] Berthold Stöger,[3] Devashibhai T. Adroja,[4,5] and Herwig Michor[1,†]

[1]*Institute of Solid State Physics, TU Wien, Wiedner Hauptstrasse 8-10, A-1040 Wien, Austria*

[2]*Institute of Nanotechnology and Materials Engineering, Faculty of Applied Physics and Mathematics and Advanced Materials Center, Gdansk University of Technology, Narutowicza 11/12, 80-233 Gdansk, Poland*

[3]*X-Ray Center, TU Wien, Getreidemarkt 9, A-1060 Wien, Austria*

[4]*ISIS Facility, Rutherford Appleton Laboratory, Chilton, Didcot Oxon OX11 0QX, United Kingdom*

[5]*Highly Correlated Matter Research Group, Physics Department, University of Johannesburg, Auckland Park 2006, South Africa*

(Received 30 September 2022; revised 18 December 2022; accepted 1 March 2023; published 17 March 2023)

Single crystals of $TmNiC_2$ were grown by the optical floating-zone technique and were investigated by x-ray diffraction (XRD), thermal expansion, electrical resistivity, specific heat, and magnetic susceptibility measurements. Single-crystal XRD reveals the formation of a commensurate charge density wave (CDW) characterized by a CDW modulation vector $\mathbf{q_{2c}} = (0.5, 0.5, 0.5)$, which is accompanied by a symmetry change from the orthorhombic space group *Amm*2 to the monoclinic space group *Cm*, i.e., to a CDW superstructure which is isostructural with that of $LuNiC_2$. For all transport and thermodynamic properties, anomalies related to a second order-type thermodynamic CDW phase transition are observed at around $T_{CDW} \simeq 375$ K. The large specific heat anomaly at T_{CDW}, $\Delta C \simeq 6.2\ \mathrm{J\,mol^{-1}K^{-1}}$, together with noticeable changes in entropy and enthalpy related to the CDW transition, suggests that this point group symmetry breaking CDW phase transition affects more significant parts of the Fermi surface as compared to the incommensurate CDW transition of, e.g., $SmNiC_2$ with no change in point group symmetry. The results on the antiferromagnetic and paramagnetic state of $TmNiC_2$ obtained by the above macroscopic techniques were complemented by microscopic studies via inelastic neutron scattering. A crystalline electric field modeling of macroscopic susceptibility and magnetic specific heat and entropy contributions as well as microscopic neutron scattering data, reveal crystal field eigenstates and eigenvalues with a ground-state doublet of the Tm-4*f* electrons, which is well separated by about 25 meV from exited states of the $J = 6$ ground-state multiplet.

DOI: 10.1103/PhysRevB.107.125137

I. INTRODUCTION

Rare-earth transition metal carbides are a unique class of intermetallic compounds where the *p*-element enters into the lattice in form of submolecules, i.e., carbon dimers, trimers or even higher multimers, rather than as individual atoms (see, e.g., Ref. [1] for a review). As a consequence of this specific crystal chemistry, quite a few of these compounds exhibit features of an effectively reduced electronic dimensionality (see, e.g., Refs. [2–4]). Among those with quasi-one-dimensional features of their electronic structure, recent interest has focused on $RNiC_2$ compounds with the noncentrosymmetric orthorhombic $CeNiC_2$-type structure [5,6], because various outstanding features have been reported: $LaNiC_2$ exhibits unconventional superconductivity [7,8], several others, e.g., $GdNiC_2$ and $TbNiC_2$, exhibit even multiple charge density wave (CDW) instabilities [9–12] and, most recently, the whole family of noncentrosymmetric rare-earth transition metal dicarbides has been highlighted for manifold topological features of their electronic structure [13]. The diversity of interesting features is further boosted by the mutual interplay of CDW features with the RKKY mediated rare-earth magnetism of $RNiC_2$ compounds [14,15] and, of course, by their potential for tuning certain topological states with external magnetic field control on the magnetic state of some of these compounds [13]. It appears, thus, relevant to further investigate the magnetic ground states of $RNiC_2$ compounds where details of crystalline electric field (CEF) eigenstates were so far provided only for $CeNiC_2$ [16].

Two distinctly different primary types of CDW superstructures of $RNiC_2$ compounds have been reported, each with its characteristic CDW modulation wave vector. Light-lanthanide compounds $RNiC_2$ with $R =$ Pr – Sm display an incommensurately modulated ground-state superstructure with a modulation wave vector $\mathbf{q_{1ic}} = (0.5, 0.5 + \delta, 0)$ [17] and, for $SmNiC_2$, it was shown that the incommensurate CDW state maintains the orthorhombic point group symmetry [18]. $YNiC_2$ and $RNiC_2$ with heavy rare-earth elements $R =$ Ho, Er, and Lu, i.e., $RNiC_2$ compounds with a smaller unit cell volume, display a commensurate CDW ground-state superstructure with modulation vector $\mathbf{q_{2c}} = (0.5, 0.5, 0.5)$ [12], which implies a reduction of the point group symmetry. For $LuNiC_2$, a detailed model of the commensurate CDW superstructure with a monoclinic space group symmetry has been reported [19].

In the case of $TmNiC_2$, CDW formation was reported on the basis of characteristic CDW anomalies of the electrical resistivity and Hall effect at $T_{CDW} \simeq 394$ K [10], however, a

*marta.roman@pg.edu.pl
†michor@ifp.tuwien.ac.at

direct investigation of the CDW superstructure, e.g., by single-crystal diffraction studies, remained pending. The magnetic properties and magnetic structure of $TmNiC_2$ were initially investigated by means of magnetic susceptibility [21,22] and powder neutron diffraction [23–25]. These studies revealed a strong uniaxial anisotropy along the a axis [22] and a simple collinear antiferromagnetic (AF) ground state with a Néel temperature $T_N = 5.5$ K [23]. Recent magnetotransport and Hall effect measurements by Kolincio *et al.* [26] suggested a coexistence of CDW order with a field polarized, saturated magnetic state in $TmNiC_2$, which stands in contrast to the effect of spontaneous ferromagnetic order in $SmNiC_2$ where Shimomura *et al.* reported an abrupt suppression of CDW superstructure reflections at temperatures right below T_C [14].

In this paper, we report on single-crystal studies of $TmNiC_2$ with a special focus on charge density wave and magnetic ground-state features. To reveal the CDW state and to determine the CDW superstructure of $TmNiC_2$, we performed single-crystal x-ray diffraction studies as well thermodynamic and transport measurements. Details of the crystalline electric field acting on the Tm-4f states are analysed by a modeling of specific heat, entropy, magnetic susceptibility and inelastic neutron scattering data.

II. EXPERIMENTAL

Polycrystalline samples of $TmNiC_2$ were synthesized by arc melting of pure elements, i.e., Tm (99.9%) and Ni (99.99%) metals, and C (graphite, 99.999%), in a high-purity argon atmosphere. An excess of about 3% of Tm and C was used to compensate losses during the arc melting procedure. In a next step, feed and seed rods of polycrystalline $TmNiC_2$ were prepared by radio-frequency induction heating under argon atmosphere (99,9999%) and these rods were finally used to grow large volume single crystals of $TmNiC_2$ via the floating zone technique in an optical mirror furnace (Crystal Systems Corporation, Japan). Obtained single crystals were oriented by means of the Laue method and cut along the orthorhombic a, b, and c orientations for specific measurements.

The initial characterization of the $TmNiC_2$ crystals was performed by means of scanning electron microscopy (SEM) using a Philips XL30 ESEM with EDAX XL-30 EDX detector as well as by powder x-ray diffraction (pXRD) studies with an *Aeris* powder diffractometer by Malvern Panalytical. Electron microprobe studies confirmed within error bars a homogeneous 1-1-2 stoichiometry with no relevant inclusions of impurities, further corroborated by pXRD where no secondary phase was resolved. The room temperature lattice parameters were determined from Pawley profile refinement of the pXRD pattern with LaB_6 NIST Standard Reference Material 660b as an internal standard using the `Panalytical HighScore Plus` software suite. The a parameter of LaB_6 was fixed to 4.15689 Å. The resulting values of lattice parameters, $a = 3.487$ Å, $b = 4.488$ Å, and $c = 6.003$ Å, of $TmNiC_2$ are in close agreement with previous reports [6,10]. The error bars were estimated as being in the fourth significant digit by freely refining the lattice parameter a of LaB_6.

Additional pXRD patterns were collected in an extended temperature interval from 300 K to 450 K using Cu K_α radiation on a Panalytical X'Pert Pro diffractometer system equipped with an Anton-Paar HTK-1200 high temperature chamber under He atmosphere. The temperature-dependent lattice parameters obtained thereby were used to extract thermal expansion data. The latter are extended towards low temperatures (in the range between 4.3 K and 315 K) via capacitive dilatometry employing a tilted plate geometry [27] on a cuboid shape single crystal of $TmNiC_2$ which was cut along its orthorhombic orientations $a \times b \times c \simeq 1.23 \times 2.54 \times 1.9$ mm^3.

TABLE I. Single-crystal data collection and structure refinement details of $TmNiC_2$. Molar mass $M = 251.66$ g/mol.

	$T = 400$ K	$T = 280$ K
Space group	*Amm*2	*Cm*
a (Å)	3.4891(4)	7.4976(9)
b (Å)	4.4898(6)	6.9675(8)
c (Å)	6.0033(8)	3.7441(5)
β (deg.)	90	106.41(1)
V (Å^3)	94.04(2)	187.62(4)
Z	2	4
Absorp. coeff. μ (mm^{-1})	56.342	56.482
D_{calcd} (g cm^{-1})	8.887	8.909
θ_{max} (°)	36.46	36.84
Reflections		
measured	884	4171
unique	253	716
observed ($I > 2\sigma(I)$)	253	683
Parameters	16	30
R_{int}	0.0327	0.0452
R ($I > 2\sigma(I)$)	0.0184	0.0446
$wR2$ (all)	0.0436	0.1342
GooF	1.163	1.149
Extinction (SHELX)	0.037(4)	—
Diff. el. density min, max (e Å^{-3})	−1.778, 2.789	−2.663, 4.441
CSD-Number	2221970	2221971

Diffraction data of plate shape crystal fragments of $TmNiC_2$ were collected on a `STOE STADIVARI` diffractometer system using Mo K_α radiation in a dry stream of nitrogen at 400 and 280 K. Data were reduced to intensity values using X-Area and scaled using the multi-scan approach implemented in LANA [28]. The 280 K data set was treated as a twin of index 2 ("HKLF5"-style reflection data with overlap information). Coordinates for the initial models were adopted from the isotypic $LuNiC_2$ structures [19]. The structures were refined with `SHELXL` [29]. In the 280 K structure, the atomic displacement parameters of the two independent C atoms were constrained to the same value. Data collection and refinement details are compiled in Table I. Further details on the crystal structure analyses can be obtained from the inorganic crystal structure database (ICSD) [30] on quoting the depository listed at the end of Table I. Complementary data of a different crystal fragment was collected at 100 K and results of refinements are available at ICSD (CSD-2221972). The reliability factors of the latter refinements were inferior to the those of data collected at 280 K and the resulting model is, thus, not discussed here in detail.

The electrical resistivity was measured with a regular four-probe technique in a commercial Quantum Design, Physical Properties Measurement System (PPMS) with thin ($\phi = 50$ μm) gold wires serving as electrical contacts which were spark welded to the polished surface of bar-shaped samples with typical dimensions $\sim 3 \times 1 \times 0.5$ mm^3.

Heat capacity data were collected with a Quantum Design PPMS using a relaxation-type method in the temperature range 2 to 400 K and additionally with a home-made calorimeter employing an adiabatic step-heating technique in the temperature interval 2 to 20 K. Apiezon-N grease was used as thermal contact medium for temperatures below 300 K, while Apiezon-H grease was applied for measurements above 300 K.

Field-dependent (0–9 T) isothermal magnetization and temperature-dependent (2–400 K) dc magnetic susceptibility studies were performed with a Quantum Design PPMS vibrating sample magnetometer (VSM) for the principal orthorhombic orientations of single-crystalline $TmNiC_2$ using the above specified cuboid-shape crystal. Molar units used in the context with heat capacity, entropy and magnetic susceptibility data stand for mol-f.u., i.e., refer to the formula unit of $TmNiC_2$.

Inelastic neutron scattering studies were conducted for $TmNiC_2$ and $LuNiC_2$, each about 10 g coarse powder of well annealed polycrystalline material, using the direct geometry time-of-flight chopper spectrometer MAPS located at the ISIS spallation neutron source at the Rutherford Appleton Laboratory, UK [31]. Powder samples were wrapped in a hollow cylinder made from thin Al-foil and mounted inside an Al-can with 40 mm diameter and 40 mm height in an annular form. The experimental temperature range down to 5 K was provided by a closed cycle refrigerator with He-exchange gas. The data were calibrated to absolute units (mbarn sr^{-1}meV^{-1} per f.u.) by means of a standard vanadium reference sample measured in identical conditions. The scattering intensities were collected in an angular range from 3.3° to 60° with an incident neutron energy of 50 meV (with a Fermi chopper frequency of 400 Hz) at four temperatures, $T \simeq 16$ K, 75 K, 150 K, and 293 K. The estimated elastic resolution was 1.49 meV and it was 1.1 meV at an energy transfer of 25 meV.

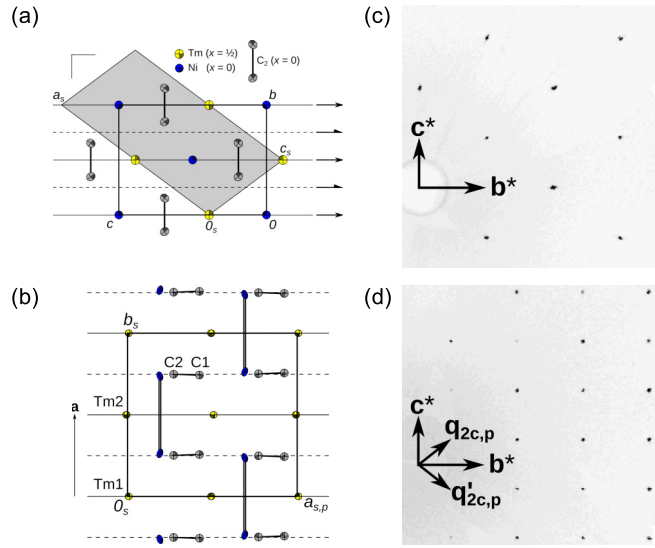

FIG. 1. (a) The high-temperature phase of $TmNiC_2$ at 400 K viewed down [100]. Tm (yellow), Ni (blue) and C (gray) atoms are represented by ellipsoids drawn at the 75% probability levels. Symmetry operations of the *Amm*2 space group are indicated using the usual graphical symbols [32]. A gray backdrop indicates the unit cell of the low-temperature superstructure. (b) The low-temperature phase of $TmNiC_2$ at 280 K viewed down [001] (corresponding to the $[01\bar{1}]$ direction of the high-temperature phase). The indicated unit-cell corresponds to the conventional setting of the low-temperature phase. A *p*-subscript indicates a vector pointing out of the drawing plane. The lattice basis vector **a** of the aristotype is indicated. (c) $h = 0$ and (d) $h = \frac{1}{2}$ sections of reciprocal space of a $TmNiC_2$ crystal at 280 K reconstructed from single-crystal XRD frame data. The reciprocal basis of the basic structure and the modulation vectors of both twin domains are indicated. A subscript "p" designates a vector projected onto the drawing plane.

III. RESULTS

A. Crystal structure determination from single-crystal XRD data

At 400 K, $TmNiC_2$ adopts the *Amm*2 aristotype structure of the $CeNiC_2$ family [see Fig. 1(a)]. Tm, Ni, and the C_2 dumbbells are all located on positions with *mm*2 site symmetry [Ni and C_2: Wyckoff position 2*a* ($x = 0$); Tm: 2*b* ($x = \frac{1}{2}$)]. Owing to the **a** translation, the Tm and Ni atoms are located on lines parallel to [100] with interatomic distances of $a = 3.4891(4)$ Å between neighboring atoms.

On cooling to 280 K, the crystals transform to a phase isotypic with the *Cm* low-temperature phase of $LuNiC_2$ [see Fig. 1(b)]. The volume of the primitive cell is doubled (ignoring metric deformations), which leads to superstructure reflections at $\mathbf{q} = \mathbf{a}^*/2 + \mathbf{b}^*/2 + \mathbf{c}^*/2$ with respect to the basis of the orthorhombic *A*-centred aristotype phase. In the conventional setting, the basis of the low-temperature superstructure is $(\mathbf{a}_s, \mathbf{b}_s, \mathbf{c}_s) = (\mathbf{b} + \mathbf{c}, 2\mathbf{a}, (\mathbf{b} - \mathbf{c})/2)$. Unless noted otherwise, all directions are given with respect to the aristotype structure, even when discussing the low-temperature phase.

The point symmetry is reduced by an index of 2 (*mm*2 to *m*). The lost point symmetry is retained as twin operation. In fact all crystals under investigation formed twins on cooling as it has already been observed for $LuNiC_2$ [19]. Whereas the basic structure reflections of both twin domains overlap perfectly [Fig. 1(c)], the satellite reflections of both domains appear at distinct positions as shown for the $(\frac{1}{2}, k, l)$ plane in Fig. 1(d).

Of the (nontranslation) symmetry elements only the $m_{[100]}$ reflections planes are retained in the superstructure. Half of the planes are still realized as proper reflection planes, whereas the other half is turned into glide reflection planes [Fig. 1(b)]. The Tm atoms split in two positions, both located on the reflection plane (Wyckoff position 2*a*) and deviate only slightly from the position in the aristotype structure [Tm–Tm distance of 3.4853(4) Å]. In contrast, there is only a single Ni-position whose site symmetry is reduced to the general position. The Ni atom is displaced significantly in the [100] direction, forming distinct pairs of Ni atoms. Adjacent atoms

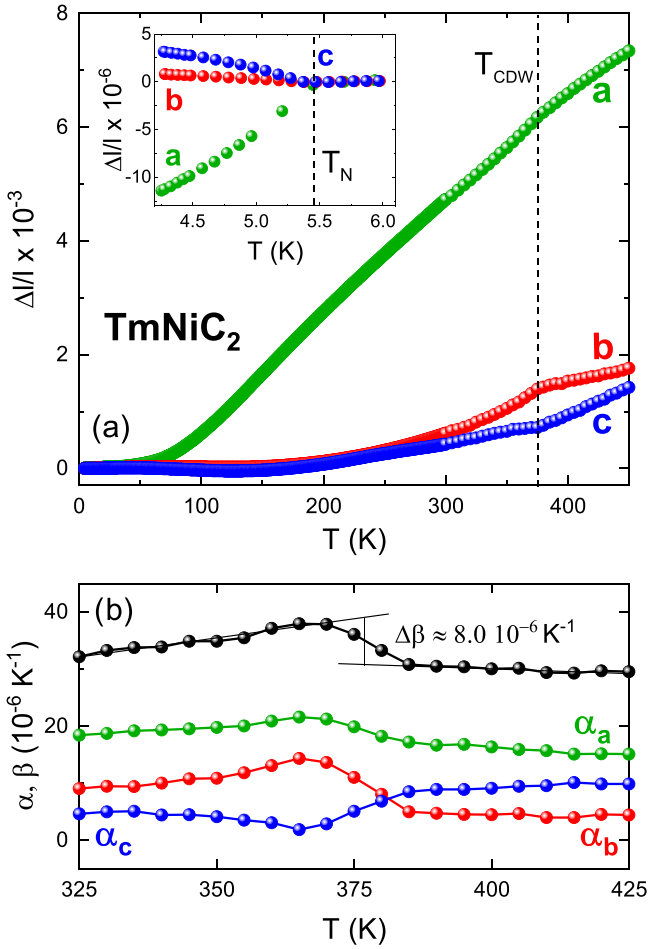

FIG. 2. (a) Temperature-dependent thermal expansion along orthorhombic a (green), b (red), and c (blue) orientations of $TmNiC_2$. Inset zooms towards the AF transition. Both, CDW and AF transition temperatures are indicated by dotted lines; (b) thermal expansion coefficients and volume expansion coefficient vs temperature. Solid lines are a guide to the eye.

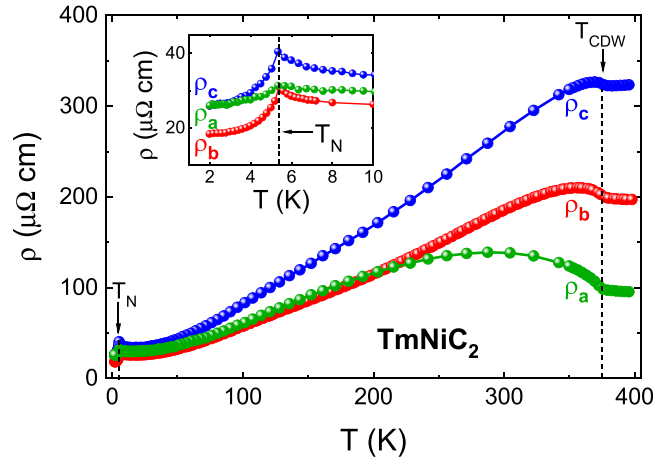

FIG. 3. Temperature-dependent electrical resistivity measured with applied current along orthorhombic a (green), b (red), and c (blue) orientations of $TmNiC_2$ single-crystal bars; solid lines are guides to the eye. Inset zooms towards the AF transition. Both CDW and AF transitions are indicated by the black arrows and dotted lines.

are related by the reflection plane, which means that the Ni–Ni pairs are perfectly parallel to [100], i.e., featuring a Peierls dimerization of the Ni atoms along the orthorhombic a axis. The short and long Ni–Ni distances at $T = 280$ K are 3.295(3) and 3.673(3) Å, respectively. This represents a deviation of 5.4% from the averaged Ni–Ni distance. Thus, the Peierls dimerization is less pronounced than in the case of $LuNiC_2$ at 100 K (6.9%) [19]. Further cooling of $TmNiC_2$ to 100 K did not increase the effect. The symmetry of the C_2 dumbbell is likewise reduced to 1, i.e., there are now two distinct C positions.

B. Thermal expansion studies

Temperature-dependent thermal expansion data were obtained by two different experimental techniques, below 315 K by capacitive dilatometry of an oriented $TmNiC_2$ single crystal and above 300 K by pXRD. These data, presented in Fig. 2(a), reveal a significantly anisotropic lattice expansion which, above 50 K, is by far largest along the orthorhombic a axis and relatively small, partly even negative, along the b and c axis. Distinct anomalies are observed: (i) the AF ordering at $T_N = 5.4$ K, which is highlighted in the inset of Fig. 2(a), and (ii) in the main panel, a structural CDW transition is pinpointed by a distinct change of the slope of each $\Delta l/l(T)$ curve at $T_{CDW} \sim 375$ K. Both transitions, AF and CDW, are manifested by kinklike features of the thermal expansion which are indicative of a second order type of these phase transitions. AF order (i) causes a contraction, as compared to the paramagnetic state, along the a axis and a minor expansion along the b and c axis, such that overall the AF-volume coupling results in a small volume reduction. Kinklike CDW transition anomalies (ii) are more pronounced and opposite along the orthorhombic b and c axis.

Temperature-dependent thermal expansion coefficients $\alpha(T)$, i.e., the temperature derivatives of $\Delta l/l$ (smoothed over four data points), together with the resulting volume expansion coefficient, $\beta(T) = \alpha_a(T) + \alpha_b(T) + \alpha_c(T)$, are presented in Fig. 2(b). Here, CDW anomalies are visible as steplike features and overall, the volume expansion coefficient displays a steplike drop $\Delta\beta \simeq 8.0 \times 10^{-6}$ K^{-1} which refers to an increase of T_{CDW} with increasing external hydrostatic pressure (see discussion in Sec. IV B for further details).

C. Electrical resistivity studies

The electrical resistivity, $\rho(T)$, measured for current parallel to the orthorhombic a-, b- and c axis of $TmNiC_2$ single-crystal bars is depicted in Fig. 3. The onset of CDW order at $T_{CDW} \simeq 375$ K is indicated for all three principal orientations by a distinct anomaly of the temperature-dependent electrical resistivity showing, upon cooling, a marked increase which refers to the opening of additional energy gaps due to new Brillouin zone boundaries caused by the symmetry reducing CDW modulation of the crystal lattice. No thermal hysteresis has been observed near T_{CDW} suggesting a second-order rather than first-order character of this phase transition. For $TmNiC_2$ single-crystal samples studied in the present work, the temperature assigned to the CDW transition, which

is determined from the local minimum of $d\rho/dT$, is found to be slightly lower than the value reported earlier for a polycrystalline sample [10]. The resistive anomalies of polycrystalline $R\mathrm{NiC}_2$ samples seem slightly broadened which is possibly the consequence of thermal strain effects caused by anisotropic thermal expansion (see above).

At high temperatures, a strong anisotropy of electrical resistivity is evident with the lowest resistivity observed for current $I||a$ axis and the highest for the $I||c$ axis. The anisotropy regime at $T > T_{\mathrm{CDW}}$, i.e., $\rho_c > \rho_b > \rho_a$, matches with the previously reported anisotropies of the electrical resistivity of SmNiC_2 [14], TbNiC_2 [9], and LuNiC_2 [19]. Below T_{CDW}, the anisotropy of the electrical resistivity of TmNiC_2 decreases and finally displays an almost isotropic character for temperatures lower than 50 K. This behavior is analogous to that observed for LuNiC_2 [19], thus indicating that the commensurate CDW transition with reduction of the space group symmetry from the orthorhombic to monoclinic one tends to alter the effective dimensionality of the electronic structure (see discussion in Ref. [19]).

At $T_{\mathrm{N}} \simeq 5.4$ K, clear anomalies of the electrical resistivity are observed for all three orientations (see inset of Fig. 3), which refer to the disappearance of spin-disorder scattering in the state of long range magnetic order. The resistivity drop, $\Delta\rho_{T_{\mathrm{N}}} = \rho(T_{\mathrm{N}}) - \rho(2\mathrm{K})$, is highly anisotropic, larger for $I||b$ and $I||c$ axis ($\Delta\rho_{T_{\mathrm{N}}} \simeq 12$ and 14 μΩcm, respectively) and smaller for $I||a$ axis ($\Delta\rho_{T_{\mathrm{N}}} \simeq 5$ μΩcm), i.e., spin scattering is large for current perpendicular and small for current parallel to the easy orientation of $4f$ magnetic moments (compare the magnetic structure reported in Ref. [23]). Above T_{N}, conduction electron spin-scattering with localized magnetic moments relates to the scattering channels of the twofold degenerate CEF ground state of the Tm $4f$ orbitals which is well separated from higher energy CEF states (see details of CEF in Sec. IV C). It is, thus, interesting to see a peaklike shape of the magnetic anomalies in $\rho(T)$, which hints at an enhancement of spin-disorder scattering due to short range magnetic correlations, which are strongest right above T_{N}. When probing spin-disorder scattering at the local minimum of $\rho(T)$, which is located at about 15 K, e.g., for $I||c$ axis which shows the strongest effect, we obtain $\Delta\rho = \rho(T_{\mathrm{N}}) - \rho(15\mathrm{K}) \simeq 7$ μΩcm, i.e., the enhancement of scatting right at T_{N} is half as large as the above given figure of $\Delta\rho_{T_{\mathrm{N}}}$.

The residual resistivity at 2 K is determined to: $\rho_{0a} \simeq \rho_{0c} \simeq 26$ μΩcm and $\rho_{0b} \simeq 18.5$ μΩcm. These values are similar to that determined for polycrystalline TmNiC_2 [26] and slightly lower than the numbers obtained from LuNiC_2 single crystals ($\rho_{0a} \sim \rho_{0c} \sim 48$ μΩcm and $\rho_{0b} \sim 32$ μΩcm) [19].

D. Specific heat results and analysis of entropy contributions

The temperature-dependent specific heat of single-crystalline TmNiC_2 and its nonmagnetic reference LuNiC_2 (see Ref. [19] for sample details) is depicted in Fig. 4(a). Close to the upper experimental temperature limit, the specific heat of TmNiC_2 reveals a pronounced second-order-type phase transition at $T_{\mathrm{CDW}} \simeq 375$ K [for a close up, see Fig. 4(b)] related to the lattice symmetry breaking charge density wave formation. The ordering temperature is in good agreement with that ones identified from thermal expansion and electrical resistivity data (see above). The specific heat jump at the CDW transition was roughly estimated as $\Delta C_p \approx 6.2\ \mathrm{J\,mol^{-1}K^{-1}}$ [see Fig. 4(b)] and, thus, yields a significant relative change $\Delta C_p/C_p(T_{\mathrm{CDW}}) \approx 6.1\%$. To determine the Tm $4f$ magnetic specific heat contribution $C_{\mathrm{mag}}(T)$, the heat capacity of LuNiC_2 was subtracted from the TmNiC_2 data, however, resulting in $\Delta C_p(T)$ [see Fig. 4(c)], which still includes a rather prominent contribution originating from the CDW phase transition. The latter is tentatively separated by a linear interpolation of the CEF Schottky anomaly in the temperature interval from 250 to 400 K [see solid blue line in Figs. 4(b) and 4(c)].

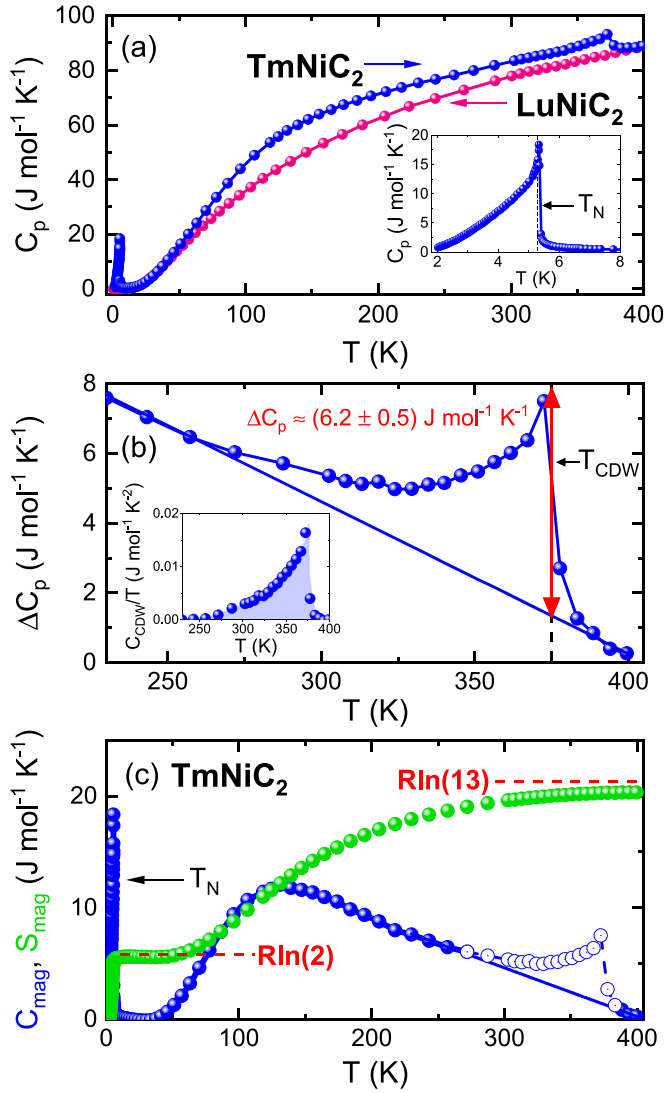

FIG. 4. (a) Temperature-dependent specific heat of TmNiC_2 (blue) and LuNiC_2 (pink) where lines connecting data points are just guides to the eye; the inset zooms in on the AF transition; (b) ΔC_p in the vicinity of the CDW transition where the straight solid line serves to extrapolate the CEF Schottky anomaly; the inset shows our estimate of the contribution C_{CDW}/T (see text); (c) temperature-dependent magnetic specific heat and entropy contributions where red dotted lines mark $S = R\ln(2J+1)$ for $J = 1/2$ and $J = 6$, respectively.

From the heat capacity in excess of this linear extrapolation line, we evaluate a rough estimate of the CDW related gain in entropy, S_{CDW}, and gain in enthalpy, H_{CDW}, by integrating the shaded area $(C_{\mathrm{CDW}}/T)dT$ in the inset of Fig. 4(b) and by integrating a corresponding area as $C_{\mathrm{CDW}}dT$, respectively. The obtained values are $S_{\mathrm{CDW}} \sim 0.6\,\mathrm{J\,mol^{-1}K^{-1}}$ and $H_{\mathrm{CDW}} \sim 210$ J/mol.

At low temperatures, a clear anomaly associated with the AF transition is visible at $T_{\mathrm{N}} = 5.4$ K [see inset of Fig. 4(a)] where the specific heat peaks at a value of $18.3\,\mathrm{J\,mol^{-1}K^{-1}}$. In Fig. 4(c), the broad maximum of the magnetic specific heat contribution $C_{\mathrm{mag}}(T)$, centered at around 125 K, manifests a Schottky anomaly due to CEF excitations within the $4f^{12}$ Hund's rules ground multiplet. The related $4f$ magnetic entropy gain $S_{\mathrm{mag}}(T)$ is shown in Fig. 4(c) as green symbols. The entropy gain associated with a doublet ground state $S = \mathrm{R}\ln 2$ (R is the gas constant) is released slightly above the Néel temperature and is followed by a wide plateau of almost zero entropy gain up to approximately 50 K, above which the magnetic entropy further increases as determined by the Schottky anomaly in $C_{\mathrm{mag}}(T)$. The latter reveals the thermal population of CEF eigenstates. Near the experimental temperature limit of 400 K, $S_{\mathrm{mag}}(T)$ approaches the maximum entropy gain expected for Tm^{3+} with its Hund's rule ground state $J = 6$ yielding $S = \mathrm{R}\ln 13 = 21.33\,\mathrm{J\,mol^{-1}K^{-1}}$.

E. Magnetic susceptibility studies

Temperature-dependent magnetic susceptibility and field-dependent isothermal magnetization studies of single-crystalline $TmNiC_2$ were reported by Koshikawa *et al.* [22]. Our present results of dc magnetic susceptibility measurements in Fig. 5 as well as our re-investigation of isothermal magnetization data (not shown) are in close agreement with these earlier reported data revealing a large anisotropy with the orthorhombic a axis being the easy axis of the Tm $4f$ moments. The only relevant discrepancy, we noticed when comparing inverse susceptibility data measured with $H||b$ and $H||c$, where data of Ref. [22] display peaklike maxima of $1/\chi_b(T)$ and $1/\chi_c(T)$ at around 50 to 60 K, while corresponding features of our present data in Fig. 5(b) display a slightly different shape as compared to the former. Considering that $\chi_a \gg \chi_b, \chi_c$, it is obvious that any small misalignment angle θ of the crystal orientation away from $H \perp a$ must result in an artefact of measured $\chi_{b,c} = \chi_{b,c}\cos^2(\theta) + \chi_a \sin^2(\theta)$. Accordingly, even when just remounting the same cuboid shape crystal for VSM measurements, we observed some variation of our $\chi_b(T)$ and $\chi_c(T)$ results due to a limited precision and reproducibility of the crystal orientation alignment, typically varying within about 3°.

Considering the above presented temperature-dependent evolution of the magnetic entropy gain, $S_{\mathrm{mag}}(T)$ [see Fig. 4(c)], i.e., a CEF ground-state doublet well separated from excited states, and the analysis in terms of a CEF model as presented in Sec. IV C, it became obvious that the intrinsic $1/\chi_b(T)$ and $1/\chi_c(T)$ shall not pass a maximum, because at least up to about 50 K, i.e., in the regime of negligible magnetic entropy gain, $1/\chi_b(T)$ and $1/\chi_c(T)$ should be essentially temperature independent. The latter is also seen for the above presented thermal expansion [see Fig. 2(a)] which is almost negligible within the temperature interval ranging from T_{N} up to about 50 K. Accordingly, we estimate the misalignment angle θ by finding the appropriate correction of χ_b or χ_c for achieving a realistic intrinsic result as indicated by dashed lines in Fig. 5(b).

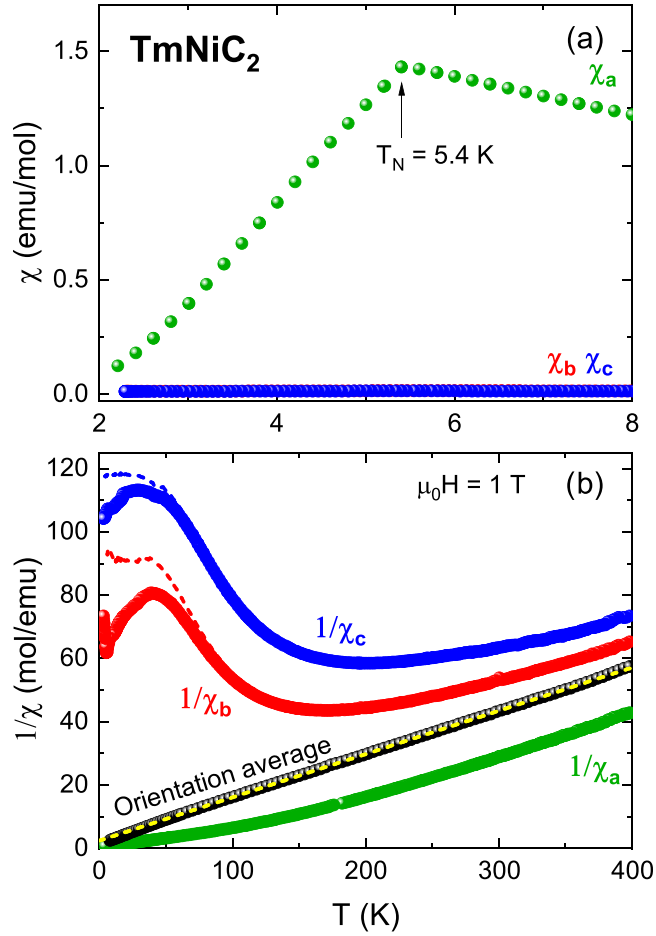

FIG. 5. (a) The temperature-dependent dc magnetic susceptibility of single-crystalline $TmNiC_2$ measured along the orthorhombic a axis orientation with an applied magnetic field of 63 mT and along the b- and c-orientations with a field of 0.1 T; (b) corresponding inverse dc susceptibility, $1/\chi$, shown for principal orientations, all measured at 1 T. The original data are shown as symbols and data of $1/\chi_b$ and $1/\chi_c$ corrected with respect to an obvious misalignment of the measured crystal (see text) are presented as dashed lines.

In Fig. 5(b), an orientation average of the single-crystal magnetic susceptibility data is plotted as $1/\chi(T)$ (black symbols) together with a Curie-Weiss fit (yellow dashed line), $\chi(T) = C/(T - \theta_p)$, on the temperature interval 240–370 K, yielding the Curie constant $C = 7.34$ emu K/mol and the paramagnetic Weiss temperature $\theta_p = -18.0$ K of $TmNiC_2$. The Curie constant is related to the effective magnetic moment $\mu_{\mathrm{eff}} = (3Ck_{\mathrm{B}}/{\mu_{\mathrm{B}}}^2 N_{\mathrm{A}})^{0.5} = 7.66\,\mu_{\mathrm{B}}$/f.u., which is in close match with the theoretical effective moment $\mu_{\mathrm{eff}} = g_J\mu_{\mathrm{B}}\sqrt{J(J+1)} = 7.56\,\mu_{\mathrm{B}}$ of the free Tm^{3+} ion.

F. Inelastic neutron scattering studies

To obtain microscopic information on CEF eigenstates and their excitation energies in $TmNiC_2$, we performed inelastic

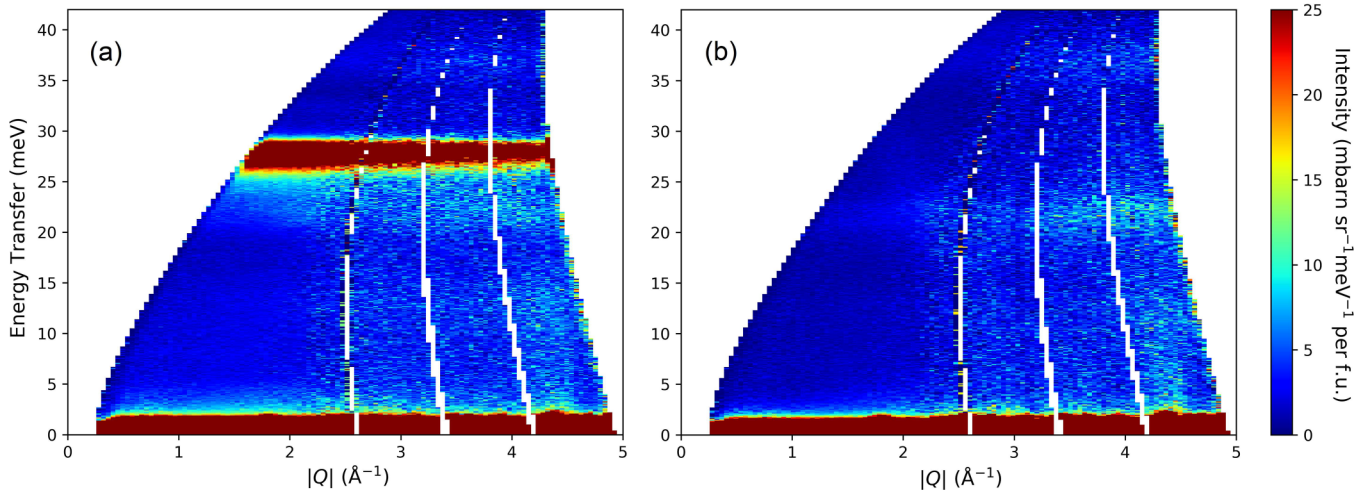

FIG. 6. Color-coded INS intensity, $I(Q, \omega)$, i.e., depending on wave vector Q and energy $\hbar\omega$ transfer, measured at $T \simeq 16$ K for (a) $TmNiC_2$ and (b) $LuNiC_2$. For the sake of better visibility of phonon intensities, high intensities are cutoff in the color coding, i.e., the actual CEF intensity of $TmNiC_2$ at around 28 meV reaches about 120 mbarn sr^{-1}meV^{-1} per f.u. at low Q.

neutron scattering (INS) studies as outlined in Sec. II. Exemplary data of wave vector- and energy-transfer-dependent scattering intensities (neutron energy loss part) are presented in Fig. 6 for $TmNiC_2$ (a) and $LuNiC_2$ (b), both measured at 16 K, i.e., well above the AF transition of $TmNiC_2$ at $T_N = 5.4$ K. $TmNiC_2$ data, as compared to the corresponding intensities collected for $LuNiC_2$, reveal a very prominent weakly Q-dependent intensity at around 28 meV, which obviously refers to the predominant CEF excitations when exciting the ground-state doublet as revealed by the above presented magnetic entropy data. For separating CEF and phonon contributions, we evaluate the magnetic scattering intensity $I_{mag}(Q, \omega)$ of $TmNiC_2$ by subtracting a properly scaled total scattering function of $LuNiC_2$ from that of $TmNiC_2$. For our fitting analysis of the inelastic CEF response of $TmNiC_2$ (see Sec. IV C), we Q-integrated the $I_{mag}(Q, \omega)$ data in an interval of scattering angles 2θ ranging from 7° to 26°, thus, yielding magnetic scattering functions $I_{mag}(\omega)$ at given experimental temperatures. The close match of the total scattering cross sections of $TmNiC_2$ and $LuNiC_2$ suggests that a scaling correction of the scattering function of $LuNiC_2$ shall be dispensable. Due to the certainly imperfectly even sample thickness distribution in our hollow cylinder sample geometry, we however noticed that, within the chosen low-Q angular integration interval, most convincing results of phonon subtraction as well as most reasonable quasielastic magnetic intensity of $TmNiC_2$ is achieved by scaling the $LuNiC_2$ inelastic data with a factor of 1.6. We emphasize, that, except for the quasielastic line intensity, this scaling correction of the $LuNiC_2$ reference data barely changes the obtained magnetic scattering functions, which peaks at about one order of magnitude higher intensity levels.

IV. DISCUSSION

A. Characteristic features of the electrical resistivity of $TmNiC_2$

As pointed out in Sec. III C, all available single-crystal resistivity data of $RNiC_2$ compounds, when measured at temperatures $T > T_{CDW}$, share the same characteristic of their orientation dependence, $\rho_c > \rho_b > \rho_a$. The latter is concordant with the quasi-one-dimensional features of the electronic structure of $RNiC_2$ compounds in their $CeNiC_2$-type parent state, which are manifested by quasiplanar, open Fermi surface sheets oriented perpendicular to the orthorhombic a axis [19,33,34]. At $T \leqslant T_{CDW}$, resistivity data of $RNiC_2$ crystals feature some distinctly different characteristics for those with an incommensurate $\mathbf{q_{1ic}} = (0.5, 0.5 + \delta, 0)$ and those with a commensurate $\mathbf{q_{2c}} = (0.5, 0.5, 0.5)$ CDW superstructure. For $TmNiC_2$ as well as $LuNiC_2$, both with a commensurate monoclinic $\mathbf{q_{2c}}$-superstructure, the most pronounced resistivity anomaly at T_{CDW} is observed for $\rho_a(T)$, whereas at the transition to the incommensurate CDW state in, e.g., $GdNiC_2$, $SmNiC_2$ and $TbNiC_2$, $\rho_c(T)$ exhibits the strongest anomaly, while that of $\rho_a(T)$ is much weaker [9,14]. Another noteworthy difference between features of the electrical resistivity in the commensurate $\mathbf{q_{2c}}$ and the incommensurate $\mathbf{q_{1ic}}$ modulated states concerns the significant change of the effective electronic dimensionality, which was pointed out earlier for $LuNiC_2$ [19], where $\rho_c > \rho_b > \rho_a$ at $T > T_{CDW}$ transforms into a more isotropic behavior, $\rho_{0c} \sim 1.5\rho_{0b} \sim \rho_{0a}$, at lowest temperatures. The latter was attributed to a fragmentation of the quasi-one-dimensional, open Fermi surface sheets of the orthorhombic parent state, which transform in the monoclinic CDW state into closed electron and hole pockets [19]. The change of the anisotropy of the electrical resistivity of $LuNiC_2$ is almost perfectly well reproduced by the present data of isostructural $TmNiC_2$, whereas earlier single-crystal resistivity studies of, e.g., $SmNiC_2$ with the incommensurate CDW state [14,18] did not reveal any significant change of the anisotropy of the electrical resistivity, neither when passing T_{CDW} nor when passing the ferromagnetic Curie temperature, T_C.

Another important aspect of the electrical resistivity concerns the interplay of magnetic and CDW order. As shown in Sec. III C, only a gentle decrease in the resistivity of $TmNiC_2$ is observed below T_N, which is in good accordance with the

result obtained earlier on polycrystalline $TmNiC_2$. For the latter, it has been assigned to a quenching of the spin disorder and a coexistence of CDW and magnetic order has been suggested [26]. On the contrary, for $RNiC_2$ (R = Nd, Sm, Gd, Tb) much larger, as compared to $TmNiC_2$, resistivity drops related to the magnetic transitions were reported. The abrupt decrease of the resistivity of the latter was attributed to a change of the spin scattering rate in the magnetically ordered state as well as to a partial (for $NdNiC_2$, $GdNiC_2$ [9,17,20,35,36]) or to a complete destruction of the CDW state by long range magnetic order as, e.g., demonstrated for $SmNiC_2$ [14].

B. Characteristic thermodynamic features of the CDW state of $TmNiC_2$

Thermodynamic characteristics of CDW phase transitions were reviewed by Saint-Paul and Monceau [37]. They analysed literature data of various CDW materials in the framework of a Landau approach for quasi-one-dimensional CDW transitions by Allender *et al.* [38] and by McMillan [39] which implies a linear relation between the magnitude of a second order-type specific heat jump ΔC_p and $T_{\rm CDW}$ via $\Delta C_p/V_{\rm mol} = A\,T_{\rm CDW}$. The latter relation can be associated with the microscopic results of a simplified BCS-type CDW model by McMillan [40] which yields $A \sim 10 N_{\rm A} N(E_{\rm F}) k_{\rm B}^2$, where $N(E_F)$ is the density of states at Fermi energy, and $N_{\rm A}$ is the Avogadro number. These relations have been tested for several CDW systems and it has been concluded that some of these systems, e.g., quasi-one-dimensional $K_{0.3}MoO_3$ and TTF-TCNQ, quasi-two-dimensional 2H-$NbSe_2$ as well as rare-earth tellurides $TbTe_3$ and $ErTe_3$, conform reasonably well with the phenomenological relation $\Delta C_p/V_{\rm mol} = A\,T_{\rm CDW}$ with A being typically of the order of 200 J K^{-2}m^{-3} [37].

Experimental data of specific heat anomalies related to second order type CDW phase transitions in $RNiC_2$ compounds were so far presented in Refs. [11,41], from which we extract $\Delta C_p \approx 1.0$ J mol^{-1}K^{-1} at a thermodynamic mean transition temperature $\overline{T}_{\rm CDW} \simeq 313$ K for $YNiC_2$ and $\Delta C_p \sim 0.6$ J mol^{-1}K^{-1} at $\overline{T}_{\rm CDW} \simeq 152$ K for $SmNiC_2$. In both cases, these CDW phase transitions are associated with a reduction of the translation symmetry, from the orthorhombic $CeNiC_2$-type parent structure to the incommensurate CDW with modulation $\mathbf{q_{1ic}} = (0.5, 0.5+\delta, 0)$ and unchanged point group symmetry. Following Ref. [37], we calculate the value of the A factor, which yields $A \simeq 110$ J K^{-2}m^{-3} and $A \sim 130$ J K^{-2}m^{-3} for $YNiC_2$ and $SmNiC_2$, respectively. The close match of the A factors implies an approximately linear scaling of the specific heat jump ΔC_p with the CDW transition temperature for these identical types of CDW phase transitions the $RNiC_2$ family. This conclusion is further corroborated by our data of, e.g., $PrNiC_2$ and $GdNiC_2$ [42], which display the same type of CDW transition to the incommensurate $\mathbf{q_{1ic}}$ superstructure.

In the following, we discuss the thermodynamic characteristics of the point group symmetry breaking, second order phase transition of $TmNiC_2$, where the orthorhombic $CeNiC_2$ high-temperature type transforms into the commensurate, monoclinic CDW superstructure.

Our results of thermal expansion and specific heat studies of $TmNiC_2$ presented in Secs. III B and III D reveal a continuous, second order phase transition and yield a thermodynamic ratio $\Delta C_p/T_{\rm CDW}V_{\rm mol} = A \simeq 580$ J K^{-2}m^{-3}, which markedly exceeds the above mentioned figures of the transitions to the incommensurate CDW state in $YNiC_2$ and $SmNiC_2$. As noted above, a mean-field weak-coupling description of the Peierls transition by McMillan [40], relates the magnitude of the A factor to the electronic density of states at the Fermi energy, $N(E_F)$. This model may, of course, require some additional factors to adapt for a specific CDW scenario (see details in Ref. [40]) and a relation $\Delta C_p \sim 10 N(E_{\rm F}) k_{\rm B}^2 T_{\rm CDW}$ is, thus, to be considered as a crude approximation. Using the DFT calculated density of states of the orthorhombic high-temperature structure of essentially isoelectronic $LuNiC_2$, $N(E_{\rm F}) \simeq 1.03$ states/eV per f.u. [19] as an estimate for $TmNiC_2$, we obtain a theoretical estimate of the specific heat jump, $\Delta C_p \sim 7$ J mol^{-1}K^{-1}, which indeed yields the correct order of magnitude of the experimental value of $\Delta C_p \simeq 6.2$ J mol^{-1}K^{-1} of $TmNiC_2$. For $RNiC_2$ with larger unit cell volume, e.g., $LaNiC_2$ and $YNiC_2$ studied in Ref. [34], DFT calculations of $N(E_{\rm F})$ yield even slightly larger values than that of $LuNiC_2$ and, accordingly, the above given specific heat anomalies of $YNiC_2$ and $SmNiC_2$ are significantly smaller than expected from the above McMillan relation, which however appears to fit well for $TmNiC_2$.

The Fermi surface of $RNiC_2$ compounds, of course, combines quasi-one-dimensional features of open Fermi surface sheets with three-dimensional features of closed electron pockets and only parts of the open (quasi-one-dimensional) Fermi surface sheets will be affected by CDW gap formation. Our DFT calculation of the electronic structure in the commensurate CDW state of $LuNiC_2$ indicated the formation of a partial gap at the Fermi energy that involves roughly about one half of the density of states, $N(E_{\rm F})$, of the parent crystal structure [19]. Corresponding DFT results of the incommensurate CDW state are still unavailable, but our above discussion of experimentally observed features with distinctly different transport characteristics of the incommensurate CDW state and the above discussion of markedly different thermodynamic ratios, $\Delta C_p/T_{\rm CDW}V_{\rm mol}$, indicate that the Fermi surface fraction affected by CDW gap formation and related Fermi surface reconstructions are very different for the incommensurate and commensurate CDW states. The reduction of the space group symmetry which is associated with the commensurate $\mathbf{q_{2c}} = (0.5, 0.5, 0.5)$ CDW modulation appears to enforce the involvement of much larger parts of the Fermi surface, as compared to the incommensurate CDW transition, and certainly causes a significant Fermi surface reconstruction (compare Ref. [19]).

Finally, we note that the magnitude of the specific heat anomaly of $TmNiC_2$ as compared to that of its volume expansion coefficient, $\Delta\beta \simeq 8.0\times10^{-6}$ K^{-1}, allows to calculate the initial response of the CDW transition temperature upon hydrostatic pressure via the thermodynamic Ehrenfest equation for second order phase transitions [43], $dT_{\rm CDW}/dp = V_{\rm mol}\,\Delta\beta\,T_{\rm CDW}/\Delta C \simeq +14$ K/GPa, i.e., it predicts an increase of $T_{\rm CDW}$ when applying hydrostatic pressure. According to the opposite sign of $\Delta\alpha_c$ as compared to that of $\Delta\beta$ [see Fig. 2(b)], an application of uni-axial pressure

along the c axis, on the contrary, should result in a reduction of T_{CDW} (compare, e.g., studies and discussion of CDW transitions in $NbSb_2$ and $Sr_3Rh_4Sn_{13}$ in Refs. [44,45], respectively).

C. Discussion of crystalline electric field effects

The CEF splitting of the $4f$ ground multiplet of rare-earth ions and their resulting CEF eigenstates impose basic constraints on the formation of long range magnetic order, i.e., on the orientation of magnetic moments and show impact also on the magnetic ordering temperature, especially in case of non-Kramers rare-earth ions with integer values of the $4f$ total angular momentum J. An initial discussion of interrelations between Néel temperatures, magnetic moment orientations and the orthorhombic CEF in RNiC$_2$ has been presented in Refs. [22,46], where CEF parameters with indices $(l, m) = (2, 0)$ and (2,2) of several RNiC$_2$ compounds were determined from the anisotropy of the high temperature magnetic susceptibility as compared to randomly oriented powder data. Thereby, Koshikawa *et al.* [22] proposed an unexpected drastic change in the evolution of these leading CEF parameters, which appeared to be much smaller for lighter-lanthanide RNiC$_2$ up to HoNiC$_2$ as compared to those of ErNiC$_2$ and TmNiC$_2$. To gain further information on the factors which govern the magnetic ground states of RNiC$_2$ compounds, we aim to analyze CEF effects in RNiC$_2$ with a detailed modeling of magnetic entropy, inverse single-crystal magnetic susceptibility and inelastic neutron scattering data, which have recently been collected for several RNiC$_2$ compounds and here, we present our analysis of the experimental data of TmNiC$_2$ introduced in Sec. III.

The monoclinic CDW superstructure modulation of TmNiC$_2$ alters the local site symmetry of the Tm ions and splits their crystallographic position into two inequivalent Tm(1)- and Tm(2)-sites and changes further the lattice periodicity within the b-c plane. The latter is accompanied by a twin-formation (see Sec. III A) which implies that for any macroscopic single-crystal measurement, the monoclinic orientations a_s and c_s [compare Fig. 1(a)] will be alternated and, thus, intermixed. Accordingly, we use the only obviously accessible, orthorhombic axis system for all macroscopic single-crystal studies, which appears still reasonable when considering the large magnetic anisotropy with the orthorhombic a axis (equal to b_s in the monoclinic stetting and unaffected by twinning) being the easy axis of CEF anisotropy and, at low temperatures, thus, very small magnetic susceptibility in orthorhombic b and c as well as monoclinic a_s and c_s orientations with large experimental error bars (see discussion in Sec. III E). The actual changes in atom coordinates as compared to the orthorhombic parent structure are rather small and expected to cause only minor changes of the CEF, as indicated by the experimental data of single-crystal inverse magnetic susceptibility data presented by Koshikawa *et al.* [22] for temperatures up to about 470 K, which did not reveal any visible trace of the CDW transition near 375 K. Accordingly, and for supporting the feasibility of the analysis, we disregard the minor in-equivalence of the two Tm-sites and analyze our experimental data in terms of the orthorhombic axis system a, b, and c, where the latter is serving as the axis of quantization, i.e., we use same scheme as Refs. [22,46]. Furthermore, we have not observed two sets of CEF excitations originating from two Tm sites and hence, the use of the orthorhombic symmetry is justifiable.

The orthorhombic CEF acting on the $4f^{12}$ orbital of Tm^{3+} with a 13-fold degenerate, $J = 6$, non-Kramers ground multiplet $^3H_6$ is described by the Hamiltonian [47]

$$\hat{\mathcal{H}}_{\mathrm{CEF}} = \sum_{l,m} A_l^m \langle r_{4f}^l \rangle \theta_l O_l^m = \sum_{l,m} B_l^m O_l^m, \tag{1}$$

where B_l^m are CEF parameters in Stevens notation and $A_l^m = B_l^m / \langle r_{4f}^l \rangle \theta_l$ are universal coefficients, i.e., CEF parameters which are independent of the rare-earth ion, θ_l are Stevens factors, $\langle r_{4f}^l \rangle$ are radial expectation values and O_l^m are the Stevens operators (for a review, see, e.g., Ref. [48]). The relevant shape factors of the Tm^{3+} $4f$ orbital, i.e., $\langle r_{4f}^l \rangle \theta_l$ are the factors $6.8727 \times 10^{-3} \times a_0^2$, $1.9165 \times 10^{-4} \times a_0^4$, and $-2.4330 \times 10^{-5} \times a_0^6$ for $l = 2$, 4, and 6, respectively, with $a_0 = 0.5292$ Å[47,49].

Initial estimates of the CEF parameters B_2^0 and B_2^2 are obtained from high-temperature magnetic susceptibility data by the same procedure as already reported in Ref. [22], i.e., from the anisotropy of the paramagnetic Curie temperatures as compared to their orientation average [50]. To determine an extended set of CEF parameters, we employ a simultaneous fitting procedure of temperature-dependent macroscopic single-crystal inverse magnetic susceptibility, heat capacity and entropy data, and microscopic powder INS magnetic scattering functions, $I_{\mathrm{mag}}(\omega)$, as determined at several temperatures. Complementing the initially estimated parameters B_2^0 and B_2^2 with additional parameters B_4^0, B_4^2 and B_4^4, we performed random walk simulated annealing fits of our combined macroscopic and microscopic data employing the `McPhase 5.3` software [51]. Finally, we multiply tested the reproducibility of fitting results by varying the initial parameters and fixing subsets of B_2^m and B_4^m while including some of the B_6^m parameters. The significance of the latter remains limited, but six out of nine parameters, B_2^0 to B_4^4 as well as B_6^0 reveal reasonable reproducibility, while B_6^2 to B_6^6 display minor relevance when fitting the present set of data.

For the initial fitting of the INS data we applied a Gaussian convolution of the calculated inelastic intensities with a constant width according to the resolution function of the MAPS spectrometer. Thereby, we noticed a temperature-dependent mismatch of calculated and experimental intensities, which revealed a significant broadening of CEF intensities measured at higher temperatures, in particular those measured at room temperature, where peak height is significantly lowered in favor of an enlarged, approximately doubled, peak width. We attribute the line-broadening at elevated temperatures to CEF-phonon interactions, which are not incorporated in the presently applied model. Another aspect neglected in our CEF model is the Tm-site splitting, which however, should have its largest effect at lower temperatures and may give rise just to a minor adjustment of the Gaussian convolution function applied for data at 16 K to a width, which is still reasonably close to the experimental resolution of the instrument. The INS data of LuNiC$_2$ presented Fig. 6(b) reveal a distinct optical phonon intensity at around 22 meV, which upon thermal

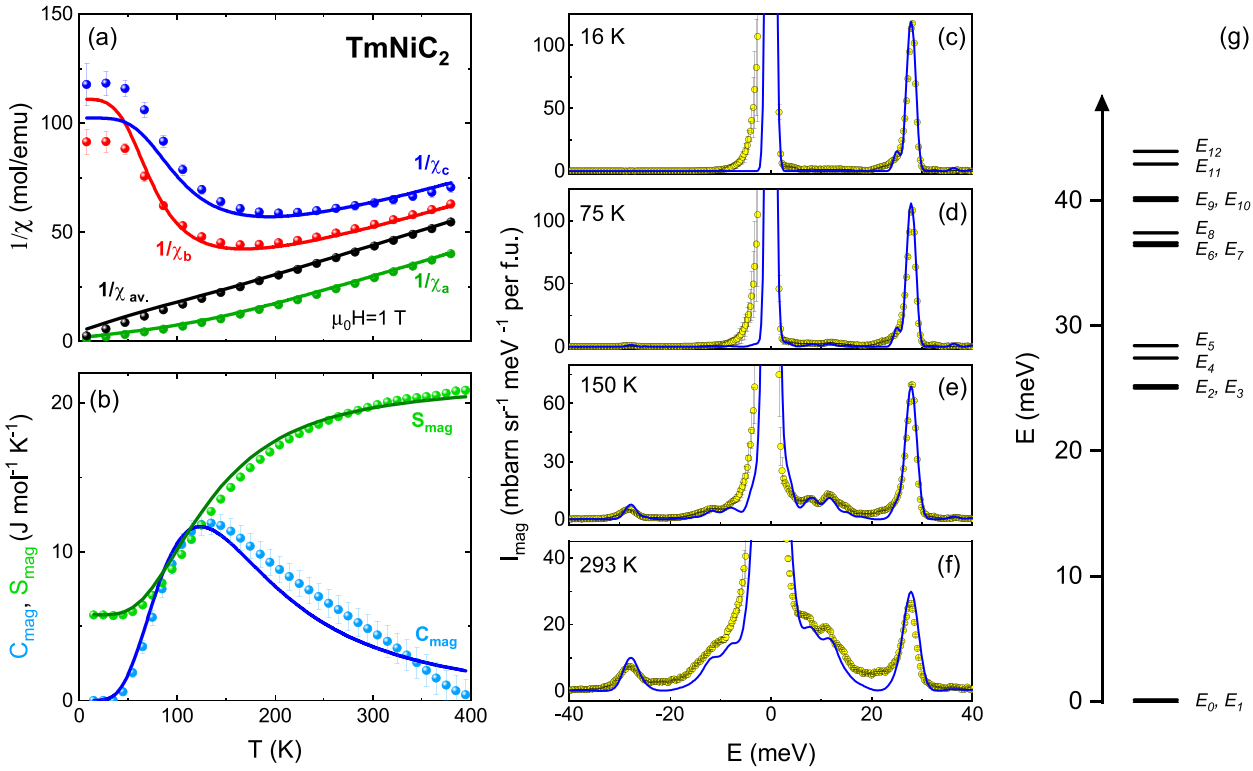

FIG. 7. (a) CEF fitting of alignment corrected inverse magnetic susceptibility data of single-crystalline $TmNiC_2$; (b) of magnetic heat capacity and magnetic entropy contributions (solid lines are fits); and (c)–(f) of magnetic scattering functions $I_{\mathrm{mag}}(\omega)$ measured at four different temperatures, where error bars of data points representing the quasielastic line are artificially enlarged by orders of magnitude to effectively exclude the quasielastic line from the fitting process; blue solid lines are calculated $I_{\mathrm{mag}}(\omega)$ functions obtained by Gaussian convolutions of the calculated magnetic scattering intensities (see text for details of the temperature variation of the applied half widths); (g) resulting CEF energy level splitting.

population may couple with CEF states centered at around 24 to 28 meV. Indeed, we observe an initial broadening and maximum peak intensity reduction for 150 K INS data, but a truly strong effect on the peak width of $I_{\mathrm{mag}}(\omega)$ data measured at room temperature. Accordingly, we obtained fits with largely reduced residual deviations by phenomenologically adjusting our Gaussian convolution functions to variable to variable line-widths, i.e., FWHM = 1.4 meV, 1.5 meV for 75 K, 2.0 meV for 150 K, and finally 3.0 meV for fitting the room temperature INS data. The resulting fits together with the experimental $I_{\mathrm{mag}}(\omega)$ data are presented in Figs. 7(a)–7(f) for inverse susceptibilities, magnetic heat capacity and magnetic entropy, and INS spectra, respectively.

Table II shows the CEF parameters as obtained from the above described fitting procedure in two most common notations and the resulting energy splitting of the CEF eigenstates. The corresponding eigenfunctions of the twofold degenerate ground state, with the orthorhombic c axis (the hard axis of CEF anisotropy) serving as quantization axis, are $|\Psi_0\rangle \simeq 0.033\,|\pm6\rangle + 0.18\,|\pm4\rangle + 0.49\,|\pm2\rangle + 0.67\,|0\rangle$ and $|\Psi_1\rangle \simeq -0.095\,|\pm5\rangle - 0.33\,|\pm3\rangle - 0.62\,|\pm1\rangle$, where $|\pm m_J\rangle$ stands for $(|m_J\rangle + |-m_J\rangle)$.

Within the typical variability of fitting results with slightly modified initial parameters, there is a minor variation of numerical factors in the above wave functions, but the specific form of the eigenfunctions forming this doublet, $|\Psi_0\rangle = a\,|\pm6\rangle + c\,|\pm4\rangle + e\,|\pm2\rangle + g\,|0\rangle$ and $|\Psi_1\rangle = -b\,|\pm5\rangle - d\,|\pm3\rangle - f\,|\pm1\rangle$ with an alphabetic sequence of monotonously increasing factors is a well reproducible result. Using a coordinate system with the easy axis of CEF anisotropy (i.e., the orthorhombic a axis) as the axis of quantization, the CEF ground-state doublet basically reads (with leading components) as $|\Psi_0\rangle \simeq -0.7\,|\pm6\rangle + 0.05\,|\pm4\rangle$ and $|\Psi_1\rangle \simeq +0.7\,|+6\rangle - 0.05\,|+4\rangle + 0.05\,|-4\rangle - 0.7\,|-6\rangle$, which manifests an Ising-like magnetic ground

TABLE II. Results of CEF parameter fitting, B_l^m in Stevens notation, universal coefficients A_l^m, and the corresponding energy level scheme (see text for details).

CEF parameters		Eigenstates
B_l^m [10^{-3} meV]	A_l^m [K/a_0^l]	energy levels [meV]
$B_2^0 = +219.9$	$A_2^0 = +371.2$	$\Delta E_{0,1} \simeq 0.0$
$B_2^2 = -328.0$	$A_2^2 = -553.6$	$\Delta E_{2,3} \simeq 25.3$
$B_4^0 = -1.047$	$A_4^0 = -63.5$	$\Delta E_4 = 27.4$
$B_4^2 = +2.743$	$A_4^2 = +166.0$	$\Delta E_5 = 28.4$
$B_4^4 = -10.01$	$A_4^4 = -605.9$	$\Delta E_{6,7} \simeq 36.4$
$B_6^0 = -0.0038$	$A_6^0 = +1.812$	$\Delta E_8 = 37.6$
$B_6^2 = +0.0070$	$A_6^2 = -3.337$	$\Delta E_{9,10} \simeq 40.4$
$B_6^4 = -0.0005$	$A_6^4 = +0.238$	$\Delta E_{11} \simeq 43.4$
$B_6^6 = -0.0029$	$A_6^6 = +1.383$	$\Delta E_{12} = 44.2$

state. It is in accordance with the observed magnetic specific heat anomaly reaching a peak value of 18.3 J mol^{-1}K^{-1} (see Sec. III D) which clearly exceeds a simple mean field expectation for the specific heat anomaly related to the ordering of magnetic moments with a multiplicity of two, which is $1.5R \simeq 12.5$ J mol^{-1}K^{-1} (compare, e.g., Ref. [52]).

Earlier reported figures of the universal coefficients $A_2^0 = +1390\,\mathrm{K}/a_0^2$ and $A_2^2 = -1760\,\mathrm{K}/a_0^2$ by Koshikawa *et al.* [22], appear to deviate significantly from the present results. However, as the underlying high temperature single-crystal susceptibility data of Ref. [22] and those of the present study are in reasonably close agreement, we suspect that the values of A_l^m provided by the former are given in units $\mathrm{K}/\mathrm{Å}^2$, because a factor $a_0^2 = 0.2801\,\mathrm{Å}^2$ would yield $A_2^0 = +389.3\,\mathrm{K}/a_0^2$ and $A_2^2 = -493.0\,\mathrm{K}/a_0^2$ and restore a reasonably close agreement with the present results.

V. CONCLUSIONS

Single crystals of $TmNiC_2$ were grown by the optical floating zone technique and studied by means of single-crystal XRD refinements revealing a commensurate, $\mathbf{q_{2c}} = (0.5, 0.5, 0.5)$ modulated CDW superstructure, which is isostructural with the monoclinic CDW superstructure reported earlier for $LuNiC_2$. The relative shortening/elongation of Ni–Ni distances, i.e., the effect of Peierls dimerization along the Ni-chains, is slightly smaller than in the case of $LuNiC_2$ with a higher $T_{CDW} \simeq 450$ K. For $TmNiC_2$, our transport and thermodynamic single-crystal studies consistently reveal a second-order-type CDW phase transition at $T_{CDW} \simeq 375$ K. Our electrical resistivity data for the principal orthorhombic orientations of $TmNiC_2$ crystals reveal an anisotropic character of the electrical resistivity in the $CeNiC_2$-type orthorhombic high temperature state, very similar to corresponding data of other $RNiC_2$ compounds. At low temperatures, however, the anisotropy of the electrical resistivity is almost completely lost and, thus, indicates a cross-over of the effective electronic dimensionality from quasi-one-dimensional at $T > T_{CDW}$ to essentially three-dimensional at low temperatures. The latter observation matches with our earlier results of $LuNiC_2$, but is clearly different from the features of the anisotropic resistivity of light-lanthanide-based $RNiC_2$ compounds, which adopt the incommensurate CDW ground state where the anisotropy of the electrical resistivity is rather preserved down to lowest temperatures. Our specific heat study of $TmNiC_2$ revealed a prominent specific heat anomaly at the commensurate CDW transition, which, as compared to available data of second-order-type specific heat anomalies to the incommensurate CDW state of, e.g., $YNiC_2$ and $SmNiC_2$, appears largely enhanced, even with respect to its normalized magnitude $\Delta C_p/T_{CDW}V_{mol}$. The latter indicates that the transition to the commensurate CDW superstructure, which is associated not only with a change in translation symmetry but in addition also with a reduction of the point group symmetry, involves much more significant fractions of the Fermi surface than the transition to the incommensurate CDW state without a change of the point group symmetry.

From a modeling of CEF effects in $TmNiC_2$ which combines a fitting of microscopic inelastic neutron scattering data as well as macroscopic magnetic heat capacity, entropy, inverse magnetic susceptibility data we determined a set of CEF parameters where at least the five leading parameters B_2^0 to B_4^4 as well as B_6^0 revealed reasonable significance and corresponding universal CEF coefficients, A_l^m, shall facilitate the initial CEF modeling of neighboring heavy-lanthanides $RNiC_2$. For $TmNiC_2$, our CEF model revealed a doublet ground state of the Tm $4f$ electrons, which is well separated by about 25 meV from excited states of the $J = 6$ ground-state multiplet. Our analysis of the inelastic neutron data may hint towards a CEF-phonon coupling effect at elevated temperatures, which deserves further attention in future CEF studies of $RNiC_2$.

Data of the ISIS neutron measurements are available in Refs. [53,54].

ACKNOWLEDGMENTS

Financial support for M.R. by Grant No. DEC-08/2021/IDUB/II.1/AMERICIUM of the AMERICIUM "Excellence Initiative-Research University" Program of the Gdansk University of Technology is gratefully acknowledged. D.T.A. thanks EPSRC UK for funding (Grant No. EP/W00562X/1). We thank Tomasz Klimczuk for giving M.R. access to laboratory facilities in the early stage of this study and for encouragement. Metallography support by Snezana Stojanovic and support with scanning electron microscopy and microprobe analysis by Monika Waas and Robert Svagera is gratefully acknowledged.

[1] V. Babizhetskyy, B. Kotur, V. Levytskyy, and H. Michor, in *Handbook on the Physics and Chemistry of Rare Earths*, edited by J. C. Bünzli and V. K. Pecharsky (Elsevier, Amsterdam, 2017), Chap. 298, pp. 1–263.

[2] R. Hoffmann, J. Li, and R. A. Wheeler, Yttrium cobalt carbide (YCoC): A simple organometallic polymer in the solid state with strong cobalt-carbon π bonding, J. Am. Chem. Soc. **109**, 6600 (1987).

[3] W. Scherer, C. Hauf, M. Presnitz, E.-W. Scheidt, G. Eickerling, V. Eyert, R.-D. Hoffmann, U.-C. Rodewald, A. Hammerschmidt, C. Vogt, and R. Pöttgen, Superconductivity in quasi-one-dimensional carbides, Angew. Chem., Int. Ed. **49**, 1578 (2010).

[4] J. H. Kim, C. Lee, and J.-H. Shim, Chemical and hydrostatic pressure effect on charge density waves of $SmNiC_2$, New J. Phys. **15**, 123018 (2013).

[5] O. I. Bodak and E. P. Marusin, Crystal structure of compounds $RNiC_2$ (R = Ce, La, Pr), Dokl. Akad. Nauk. Ukr. SSR. Ser. A **12**, 1048 (1979).

[6] W. Jeitschko and M. Gerss, Ternary carbides of the rare earth and iron group metals with $CeCoC_2$- and $CeNiC_2$-type structure, J. Less-Common Met. **116**, 147 (1986).

[7] A. D. Hillier, J. Quintanilla, and R. Cywinski, Evidence for Time-Reversal Symmetry Breaking in the Noncentrosymmetric Superconductor $LaNiC_2$, Phys. Rev. Lett. **102**, 117007 (2009).

[8] J. Quintanilla, A. D. Hillier, J. F. Annett, and R. Cywinski, Relativistic analysis of the pairing symmetry of the noncentrosymmetric superconductor $LaNiC_2$, Phys. Rev. B **82**, 174511 (2010).

[9] S. Shimomura, C. Hayashi, N. Hanasaki, K. Ohnuma, Y. Kobayashi, H. Nakao, M. Mizumaki, and H. Onodera, Multiple charge density wave transitions in the antiferromagnets $RNiC_2$ (R= Gd, Tb), Phys. Rev. B **93**, 165108 (2016).

[10] M. Roman, J. Strychalska-Nowak, T. Klimczuk, and K. K. Kolincio, Extended phase diagram of $RNiC_2$ family: Linear scaling of the Peierls temperature, Phys. Rev. B **97**, 041103(R) (2018).

[11] K. K. Kolincio, M. Roman, and T. Klimczuk, Charge density wave and large nonsaturating magnetoresistance in $YNiC_2$ and $LuNiC_2$, Phys. Rev. B **99**, 205127 (2019).

[12] H. Maeda, R. Kondo, and Y. Nogami, Multiple charge density waves compete in ternary rare-earth nickel carbides, $RNiC_2$ (*R*: Y, Dy, Ho, and Er), Phys. Rev. B **100**, 104107 (2019).

[13] R. Ray, B. Sadhukha, M. Richter, J. I. Facio, and J. van den Brink, Tunable chirality of noncentrosymmetric magnetic Weyl semimetals in rare-earth carbides, npj Quantum. Mater. **7**, 19 (2022).

[14] S. Shimomura, C. Hayashi, G. Asaka, N. Wakabayashi, M. Mizumaki, and H. Onodera, Charge-Density-Wave Destruction and Ferromagnetic Order in $SmNiC_2$, Phys. Rev. Lett. **102**, 076404 (2009).

[15] K. K. Kolincio, K. Gornicka, M. J. Winiarski, J. Strychalska-Nowak, and T. Klimczuk, Field induced suppression of charge density wave in $GdNiC_2$, Phys. Rev. B **94**, 195149 (2016).

[16] A. Bhattacharyya, D. T. Adroja, A. M. Strydom, A. D. Hillier, J. W. Taylor, A. Thamizhavel, S. K. Dhar, W. A. Kockelmann, and B. D. Rainford, μSR and inelastic neutron scattering investigations of the noncentrosymmetric antiferromagnet $CeNiC_2$, Phys. Rev. B **90**, 054405 (2014).

[17] N. Yamamoto, R. Kondo, H. Maeda, and Y. Nogami, Interplay of charge-density wave and magnetic order in ternary rare-earth nickel carbides, $RNiC_2$ (R = Pr and Nd), J. Phys. Soc. Jpn. **82**, 123701 (2013).

[18] A. Wölfel, L. Li, S. Shimomura, H. Onodera, and S. van Smaalen, Commensurate charge-density wave with frustrated interchain coupling in $SmNiC_2$, Phys. Rev. B **82**, 054120 (2010).

[19] S. Steiner, H. Michor, O. Sologub, B. Hinterleitner, F. Höfenstock, M. Waas, E. Bauer, B. Stöger, V. Babizhetskyy, V. Levytskyy, and B. Kotur, Single-crystal study of the charge density wave metal $LuNiC_2$, Phys. Rev. B **97**, 205115 (2018).

[20] M. Roman, T. Klimczuk, and K. K. Kolincio, Correlation between charge density waves and antiferromagnetism in $Nd_{1-x}Gd_xNiC_2$ solid solutions, Phys. Rev. B **98**, 035136 (2018).

[21] P. Kotsanidis, J. Yakinthos, and E. Gamari-Seale, Magnetic properties of the ternary carbides of the rare earth and nickel group metals, J. Less-Common Met. **152**, 287 (1989).

[22] Y. Koshikawa, H. Onodera, M. Kosaka, H. Yamauchi, M. Ohashi, and Y. Yamaguchi, Crystalline electric fields and magnetic properties of single-crystalline $RNiC_2$ compounds (R = Ho, Er and Tm), J. Magn. Magn. Mater. **173**, 72 (1997).

[23] J. Yakinthos, P. Kotsanidis, W. Schäfer, and G. Will, Magnetic structure determination of $NdNiC_2$ and $TmNiC_2$ by neutron diffraction, J. Magn. Magn. Mater. **89**, 299 (1990).

[24] W. Schäfer, G. Will, J. Yakinthos, and P. Kotsanidis, Neutron diffraction study of $RNiC_2$ (R = rare earth) compounds, J. Alloys Compd. **180**, 251 (1992).

[25] W. Schäfer, W. Kockelmann, G. Will, J. Yakinthos, and P. Kotsanidis, Magnetic structures of rare earths R in $RCoC_2$ and $RNiC_2$ compounds, J. Alloys Compd. **250**, 565 (1997).

[26] K. K. Kolincio, M. Roman, and T. Klimczuk, Enhanced Mobility and Large Linear Nonsaturating Magnetoresistance in the Magnetically Ordered States of $TmNiC_2$, Phys. Rev. Lett. **125**, 176601 (2020).

[27] M. Rotter, H. Müller, E. Gratz, M. Doerr, and M. Loewenhaupt, A miniature capacitance dilatometer for thermal expansion and magnetostriction, Rev. Sci. Instrum. **69**, 2742 (1998).

[28] STOE & Cie GmbH, *X-Area and LANA* (Darmstadt, Germany, 2022).

[29] G. M. Sheldrick, Crystal structure refinement with SHELXL, Acta Cryst. C **71**, 3 (2015).

[30] Inorganic Crystal Structure Database (ICSD), Fachinformationszentrum Karlsruhe, (Eggenstein-Leopoldshafen, Germany, 2022).

[31] R. A. Ewings, J. R. Stewart, T. G. Perring, R. I. Bewley, M. D. Le, D. Raspino, D. E. Pooley, G. Skoro, S. P. Waller, D. Zacek, C. A. Smith, and R. C. Riehl-Shaw, Upgrade to the maps neutron time-of-flight chopper spectrometer, Rev. Sci. Instrum. **90**, 035110 (2019).

[32] T. Hahn and M. I. Aroyo, Symbols of symmetry elements, in *Space-group Symmetry*, International Tables For Crystallography Vol. A (IUCr, Chester, 2016), Chap. 2.1.2, pp. 144–148.

[33] J. Laverock, T. D. Haynes, C. Utfeld, and S. B. Dugdale, Electronic structure of $RNiC_2$ (R = Sm, Gd, and Nd) intermetallic compounds, Phys. Rev. B **80**, 125111 (2009).

[34] Y. Hirose, T. Kishino, J. Sakaguchi, Y. Miura, F. Honda, T. Takeuchi, E. Yamamoto, Y. Haga, H. Harima, R. Settai, and Y. Onuki, Fermi surface and superconducting properties of noncentrosymmetric $LaNiC_2$, J. Phys. Soc. Jpn. **81**, 113703 (2012).

[35] N. Hanasaki, S. Shimomura, K. Mikami, Y. Nogami, H. Nakao, and H. Onodera, Interplay between charge density wave and antiferromagnetic order in $GdNiC_2$, Phys. Rev. B **95**, 085103 (2017).

[36] K. K. Kolincio, M. Roman, M. J. Winiarski, J. Strychalska-Nowak, and T. Klimczuk, Magnetism and charge density waves in $RNiC_2$ (R = Ce, Pr, Nd), Phys. Rev. B **95**, 235156 (2017).

[37] M. Saint-Paul and P. Monceau, Phenomenological approach of the thermodynamic properties of the charge density wave systems, Philos. Mag. **101**, 598 (2021).

[38] D. Allender, J. W. Bray, and J. Bardeen, Theory of fluctuation superconductivity from electron-phonon interactions in pseudo-one-dimensional systems, Phys. Rev. B **9**, 119 (1974).

[39] W. L. McMillan, Landau theory of charge-density waves in transition-metal dichalcogenides, Phys. Rev. B **12**, 1187 (1975).

[40] W. L. McMillan, Microscopic model of charge-density waves in $2h-TaSe_2$, Phys. Rev. B **16**, 643 (1977).

[41] G. Prathiba, I. Kim, S. Shin, J. Strychalska, T. Klimczuk, and T. Park, Tuning the ferromagnetic phase in the CDW compound $SmNiC_2$ via chemical alloying, Sci. Rep. **6**, 26530 (2016).

[42] H. Michor, M. Roman, M. Fritthum, E. Morineau, L. Reisinger, and B. Stöger, Single crystal studies of charge density wave physics in quasi-1D metals $RNiC_2$, *Book of Abstracts*, International Conference on Strongly Correlated Electron Systems, SCES 2022 (Amsterdam, The Netherlands, 2022).

[43] P. Ehrenfest, Phasenumwandlungen im üblichen und erweiterten Sinn, classifiziert nach den entsprechenden Singularitäten des thermodynamischen Potentiales, Proc. R. Acad. Amsterdam **36**, 153 (1933).

[44] V. Eremenko, V. Sirenko, V. Ibulaev, J. Bartolomé, A. Arauzo, and G. Remenyi, Heat capacity, thermal expansion and pressure derivative of critical temperature at the superconducting and charge density wave (CDW) transitions in $NbSe_2$, Physica C **469**, 259 (2009).

[45] C. N. Kuo, C. W. Tseng, C. M. Wang, C. Y. Wang, Y. R. Chen, L. M. Wang, C. F. Lin, K. K. Wu, Y. K. Kuo, and C. S. Lue, Lattice distortion associated with Fermi-surface reconstruction in $Sr_3Rh_4Sn_{13}$, Phys. Rev. B **91**, 165141 (2015).

[46] H. Onodera, Y. Koshikawa, M. Kosaka, M. Ohashi, H. Yamauchi, and Y. Yamaguchi, Magnetic properties of single-crystalline $RNiC_2$ compounds ($R =$ Ce, Pr, Nd, and Sm), J. Magn. Magn. Mater. **182**, 161 (1998).

[47] M. T. Hutchings, Point-charge calculations of energy levels of magnetic ions in crystalline electric fields, *Solid State Physics*, Vol. 16 (Academic Press, San Diego, CA, 1964), pp. 227–273.

[48] J. Jensen and A. R. Mackintosh, *Rare Earth Magnetism* (Clarendon Press, Oxford, 1991).

[49] A. Abragam and B. Bleaney, *Electron Paramagnetic Resonance of Transition Ions* (Oxford University Press, 2012).

[50] G. J. Bowden, D. S. P. Bunbury, and M. A. H. McCausland, Crystal fields and magnetic anisotropy in the molecular field approximation. I. General considerations, J. Phys. C: Solid State Phys. **4**, 1840 (1971).

[51] M. Rotter, Using McPhase to calculate magnetic phase diagrams of rare earth compounds, J. Magn. Magn. Mater. **272-276**, E481 (2004).

[52] L. De Jongh and A. Miedema, Experiments on simple magnetic model systems, Adv. Phys. **50**, 947 (2001).

[53] H. Michor and D. T. Adroja, Studies of crystalline electric field excitations of $TmNiC_2$ by inelasic neutron scattering, STFC ISIS Neutron and Muon Source, https://doi.org/10.5286/ISIS.E.RB2090132-1.

[54] H. Michor and D. T. Adroja, Inelastic neutron scattering on phonon reference $LuNiC_2$ supporting studies of CEF in $TmNiC_2$, STFC ISIS Neutron and Muon Source, https://doi.org/10.5286/ISIS.E.RB2090131-1.